PAPER • OPEN ACCESS

ITG turbulence in gyrokinetic simulations of high collisionality spherical tokamak plasmas

View the article online for updates and enhancements.

ITG turbulence in gyrokinetic simulations of high collisionality spherical tokamak plasmas

N. Kumar[1,*] ⓘ, G. Avdeeva[2] ⓘ, J. Candy[2] ⓘ, M. Reynolds[1] ⓘ, E. Belli[2] ⓘ and C.P. McNally[1] ⓘ

[1] General Fusion Inc., Richmond, British Columbia, Canada
[2] General Atomics, San Diego, CA, United States of America

E-mail: neeraj.kumar@generalfusion.com

CrossMark

Abstract

This paper presents a first detailed gyrokinetic analysis with the goal of understanding the dominant turbulent transport mechanisms and identifying the micro-instabilities present in small-aspect-ratio plasmas in the PI3 device, developed as magnetized target fusion targets. These plasmas are characterized by low temperatures and high collisionality compared to standard tokamaks. Linear and ion-scale nonlinear gyrokinetic flux tube simulations are performed at radial positions $r/a = 0.60$, 0.65, 0.70, and 0.75 using the gyrokinetic code CGYRO (Candy *et al* 2016 *J. Comput. Phys.* **324** 73). Linear stability analysis finds that ion temperature gradient (ITG) modes dominate at ion scales, while electron-temperature gradient modes dominate at electron scales. Trapped electron modes (TEMs) remain stable due to high collisionality. At very low $k_y\rho_s$, microtearing modes (MTMs) are linearly unstable at all radial locations. In the nonlinear regime, turbulence is driven primarily by ITG modes, which dominate both ion and electron energy fluxes. Interestingly, although MTMs are linearly unstable, they are suppressed in the nonlinear phase, except for a small, negative magnetic flutter contribution at the outer radius ($r/a = 0.75$) that slightly reduces the total electron energy flux. The sensitivity of these instabilities to key plasma parameters is investigated. High collisionality significantly reduces nonlinear turbulent fluxes, and lowering collisionality results in a stronger flux increase than an equivalent increase in plasma beta does. Increasing the T_i/T_e ratio in the linear analysis stabilizes ITG modes, while simultaneously destabilizing long-wavelength MTMs. Finally, turbulent energy fluxes are compared to neoclassical transport values simulated using NEO (Belli *et al* 2008 *Plasma Phys. Control. Fusion* **50** 095010), showing transport is anomalous at all radii.

Keywords: magnetized target fusion, spherical tokamak, turbulent transport, ITG, gyrokinetic

(Some figures may appear in colour only in the online journal)

---

* Author to whom any correspondence should be addressed.

1

1. Introduction

General Fusion is developing magnetized target fusion (MTF) as a technology for power generation [1]. In this form of MTF, a spherical tokamak target plasma is compressed rapidly (in a few tens of milliseconds) by electrically conducting walls on a time scale shorter than its own thermal energy confinement time. The compression thus produces close to adiabatic heating in the plasma, bringing it to fusion conditions.

Because in MTF the plasma is primarily heated by adiabatic compression, compressive heating competes with energy and particle losses due to transport. Therefore, understanding transport phenomena and dominant micro-instabilities in the relatively low-temperature, pre-compression target plasma is just as important as in high-temperature plasmas and is critical for the design of a successful MTF machine.

General Fusion has conducted a sequence of subscale compression experiments (Plasma Compression Science [2]), to understand the behavior of magnetized plasma during rapid compression using a simple implementation involving single-use solid liner compression. To develop compression-compatible plasma formation technology and study plasma targets, General Fusion has operated a meter-scale device Plasma Injector 3 (PI3) [3, 4], which succeeded the Plasma Injector 1 [5] and 2 devices, as well as a series of subscale devices termed SPECTOR [6, 7]. PI3 forms spherical tokamak plasmas by coaxial helicity injection (CHI) into a spherical chamber with tight-fitting lithium-coated aluminum walls. These plasmas are appropriate for compression as targets in an MTF machine [4].

In standard tokamak devices, the experimentally observed transport level is typically much higher than that of neoclassical collisional transport. Turbulent transport driven by micro-instabilities is known to be mainly responsible for this discrepancy and is one of the biggest sources of energy and particle losses from the system. Nonlinear gyrokinetic theory [8, 9] has been used widely to characterize turbulent transport in fusion plasmas. Gyrokinetic models have been used in many tokamaks including Alcator C-Mod [10], DIII-D [11], AUG [12], and JT-60U [13] to study and predict thermal transport losses and improve plasma performance.

In this work, we present the first thermal transport analysis of PI3 plasmas to characterize the dominant turbulent transport mechanisms and identify the micro-instabilities present in the system, using linear and nonlinear gyrokinetic simulations performed with the code CGYRO [14, 15]. Here, gyrokinetic analysis has been extended to the unique plasma conditions of PI3, where plasma has high collisionality and low temperature compared to standard tokamaks. In the present analysis, we observe that transport is predominantly driven by ion temperature gradient turbulence, while trapped electron modes are suppressed due to high collisionalities. Additionally, micro-tearing modes (MTMs) are found to be linearly unstable at very small wavenumbers, however, they are suppressed in the nonlinear phase and do not contribute significantly to transport fluxes. This behavior contrasts with other spherical tokamaks, such as NSTX, where energy transport is typically dominated by MTMs or by kinetic ballooning modes (KBMs) [16, 17]. For this study, we focus on PI3 discharge 18669, which has been identified as a suitable initial plasma target for future compression scenarios in an MTF machine. We also compare the simulated turbulence fluxes with neoclassical transport calculated using NEO [18] to quantify the level of anomalous transport.

The rest of paper is organized as follows: in section 2 a brief overview of PI3 experiment and plasma profile extraction procedure is given. In section 3 the gyrokinetic simulations setup is described. In section 4 the linear stability analysis is presented. In section 5 the nonlinear analysis is described. In section 6 sensitivity of nonlinear turbulent fluxes and linear growth rate to input parameters is investigated. Section 7 compares turbulent fluxes with neoclassical calculations. Finally, the summary and conclusions are presented in section 8.

2. Experimental analysis

2.1. PI3 device and diagnostics

PI3 is a small-aspect-ratio experimental fusion device at general fusion which forms a spherical tokamak plasma using CHI by a magnetized coaxial plasma gun (Marshall gun) [4]. Its typical magnetic flux surface shapes in cylindrical (R, Z) coordinates are shown in figure 1. It is designed to study and improve the stability and confinement of target plasmas that will be compressed in future MTF machines. PI3 is a non-compressing device with a solid lithium plasma facing surface, formed by evaporating lithium onto aluminum. Unlike PI3, the MTF power-plant machine will have liquid lithium walls to enable repeatable compression, neutron shielding, and tritium breeding. In PI3, plasmas are heated by the CHI formation process and ohmically heated by the decay of toroidal plasma current [3, 4]. Additionally, there is no external particle fueling. The only fueling is the initial fueling from the gas puff in the plasma formation region. Thomson scattering measurements indicate that the core (peak) electron temperature is $T_e \sim 250 - 400 \, eV$. Ion temperatures are measured via single-chord Ion Doppler Spectroscopy (IDS) on carbon impurity line radiation with a view of the plasma core.

Typical plasma parameters of PI3 are listed and compared with other toroidal fusion devices in table 1. PI3 has an aspect ratio similar to that of NSTX and MAST, and values of ρ^* (ion Larmor radius normalized to the plasma minor radius) comparable to those of the other devices. The value of ν_e^* (normalized collisionality as defined in equation (3)) is much higher in PI3 than the other devices, primarily due to the absence of additional external heating. Since heating in MTF is achieved through subsequent compression of a PI3-like plasma, understanding transport in this initially low-temperature state is essential for determining the plasma's ability to reach fusion conditions.
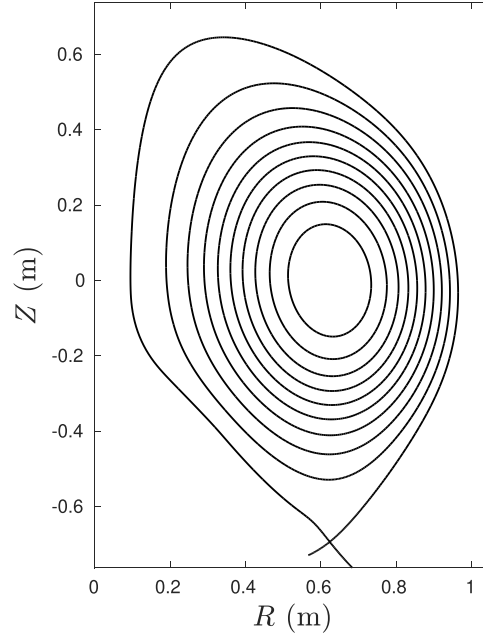
Figure 1. Magnetic flux surface geometry, in cylindrical (R, Z) coordinates, for PI3 discharge 18669 at $t = 5$ ms with magnetic axis at $Z = 0$.

Table 1. Typical plasma parameters for PI3 and comparisons with other toroidal fusion devices are presented. Here, a is the plasma minor radius, R_0 is the geometric major radius, $A = R_0/a$ is the aspect ratio, B_T is the vacuum toroidal magnetic field at R_0 from the axis of the machine, I_p is the plasma current, $\bar{n}_e$ is the line averaged electron density, T_e is the core electron temperature, λ_{De} is the electron Debye length, $\nu_{ee} = \frac{\sqrt{2}\pi e^4 n_e}{m_e^{1/2} T_e^{3/2}} \ln \Lambda$ is the electron–electron collision frequency, $\nu_e^* = (a/c_s)\nu_{ee}$ is the normalized electron collision frequency [14], ρ_i is the effective ion Larmor radius, Ω_i is the ion cyclotron frequency, and ω_i is the fluctuation frequency. These parameters are evaluated at the magnetic axis. The MAST parameters are calculated from [19], NSTX from [20], DIII-D from [21], and JET from [22].

Parameter	Units	PI3	MAST	NSTX	DIII-D	JET
a	m	0.43	0.65	0.61	0.50	1.0
R_0	m	0.62	0.85	0.86	1.67	3.0
$A = R_0/a$	—	1.44	1.30	1.40	3.34	3.0
B_T	T	0.36	0.62	0.44	2.0	3.5
I_p	MA	0.2	1.2	0.6	1.2	2.5
$\bar{n}_e$	m^{-3}	1.85×10^{19}	1.0×10^{20}	2.4×10^{19}	5×10^{19}	5×10^{19}
T_e	keV	0.35	3.0	0.7-0.8	7.0	5-15
$\lambda_{De} = \sqrt{\frac{\epsilon_0 T_e}{n_e e^2}}$	m	3.25×10^{-5}	4.1×10^{-5}	4.01×10^{-5}	8.8×10^{-5}	7.43×10^{-4}
ν_{ee}	s^{-1}	1.6×10^5	3.8×10^4	7.7×10^4	5.7×10^3	9.3×10^3
$\nu_e^* = (a/c_s)\nu_{ee}$	—	0.52	0.06	0.25	0.0049	0.019
$v_{thi} = \sqrt{T_i/m_i}$	m/s	1.31×10^5	3.7×10^5	1.83×10^5	5.79×10^5	4.89×10^5
$\rho_i = v_{thi}/\Omega_i$	m	7.0×10^{-2}	1.27×10^{-2}	8.68×10^{-3}	6.04×10^{-3}	2.91×10^{-3}
$\Omega_i = eB/m_i c$	s^{-1}	1.72×10^7	2.96×10^7	2.1×10^7	9.6×10^7	1.67×10^8
$\omega_i = v_{thi}/a$	s^{-1}	3.03×10^5	5.83×10^5	3.0×10^5	1.16×10^6	4.89×10^5
$\rho^* = \rho_i/a$	—	1.76×10^{-2}	1.96×10^{-2}	1.42×10^{-2}	1.21×10^{-2}	2.9×10^{-3}

2.2. Magnetic equilibrium reconstruction and radial plasma profiles

In this study, we selected a high-performance lithium-coated PI3 discharge 18669, where the plasma is formed using deuterium gas. This was the 10th discharge after an evaporative lithium coating of the PI3 vessel. Figure 2 presents a time series of various plasma parameters for this discharge. A time slice at 5 ms was chosen for the present gyrokinetic analysis, corresponding to the acquisition time of Thomson scattering

T_e data. Vertical dashed lines in figure 2 indicate this selected time slice. We have chosen this discharge since it is well diagnosed and shows no significant MHD activity around the time of interest. Moreover, this PI3 shot is a representative initial plasma target among other lithium-coated shots identified for compression in future MTF machines, due to its stability and favorable plasma properties.

For gyrokinetic analysis, we need radial profiles of flux surface shapes to describe the magnetic geometry and of input plasma parameters (density and temperature) as a function
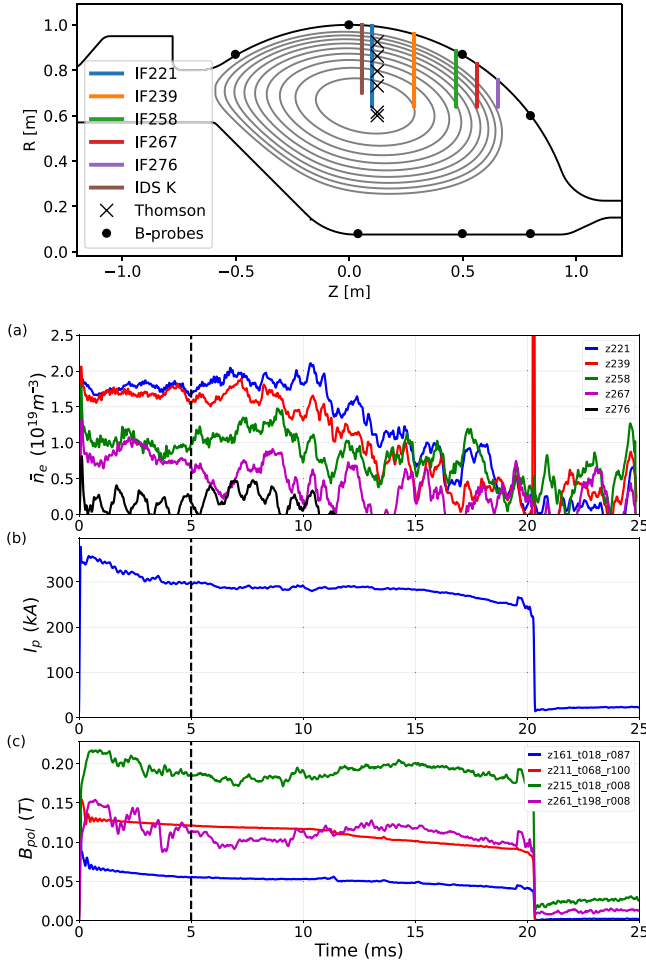
Figure 2. Time series of some plasma parameters of PI3 discharge 18669 studied in this work. Top: Cross-section of PI3 in the (R, Z) plane, showing the vessel (black outline), B-probes (black dots), interferometer (IF) chords, the IDS chord, and TS measurement points (crosses). Panel (a): line average electron density $\bar{n}_e$ vs time as measured by interferometer chords at different locations, with z221 and z276 corresponding to core and edge positions. Panel (b): plasma current vs time. Panel (c): poloidal magnetic field B_{pol} vs time as measured by B-probes. The dashed vertical line shows the TS acquisition time, $t = 5$ ms, used for gyrokinetic analysis in this paper.

of radial coordinates r/a (normalized minor radius) or $\rho_N = \sqrt{\Phi/\Phi_{LCFS}}$ (the normalized toroidal flux coordinate), where Φ represents the toroidal flux enclosed by a given flux surface and Φ_{LCFS} is the toroidal flux enclosed by the last closed flux surface (LCFS). For the PI3 device, General Fusion has implemented a data processing pipeline including a magnetic reconstruction system using a Bayesian approach [4]. In this system, a large space of possible Grad–Shafranov equilibria is parameterized and pre-tabulated, and the Bayes rule is used to determine the most probable state of the plasma given the measurement data. This Bayesian reconstruction is used for the magnetic geometry.

For the density and temperature profiles we use simple functional fits to experimental data. We take the flux surface geometry $\bar{\psi}(R, Z)$ from the initial magnetic reconstruction,

where $\bar{\psi}$ is the usual normalized poloidal flux coordinate with $\bar{\psi} = 0$ at the magnetic axis and $\bar{\psi} = 1$ at the LCFS. Then the plasma density profiles $n_e(\bar{\psi})$ and temperature profiles $T_e(\bar{\psi})$ are obtained from experimental interferometer and Thomson scattering data by least-squares fitting a simple model as follows.

We find that the interferometer data for discharge 18669 at 5 ms is reasonably well modeled by assuming the electron density varies spatially with $\bar{\psi}^2$ within the plasma, with a transition to lower density at the edge. Therefore, we adopt a forward model that expresses the density profile as:

$$n_e(\bar{\psi}) = (c_1 + c_2\bar{\psi}^2)f(\bar{\psi} - 1) + c_3 f(1 - \bar{\psi}) \qquad (1)$$

where a Fermi function $f(x) = [1 + \exp(\gamma x)]^{-1}$ is used to smooth the edge transition. The edge steepness parameter is chosen to be $\gamma = 20$.

The forward model (1) for density as a function of $\bar{\psi}$ generates synthetic (model) interferometer data for chord k via the chord-averaging operation:

$$\bar{n}_e^{mod}(k) = \frac{1}{L_k} \int n_e(\bar{\psi}(\mathbf{x})) \, ds \qquad (2)$$

where the L_k is the length of chord k, the path integral is along the line of sight of the chord, and $\bar{\psi}(\mathbf{x})$ indicates the flux surface encountered at position $\mathbf{x}$ along the chord, obtained from the 2D $\psi(R, Z)$ field from the initial magnetic reconstruction. The coefficients c_i that determine the forward model are then found by a least-squares fit to the interferometer data. This gives the density profile shown in figure 3(*a*). This figure also shows the fit of the synthetic chord average density to the values determined experimentally.

To obtain radial temperature profiles, we fit a quadratic function $T_e(\bar{\psi})$ to the Thomson scattering measurements, giving the fit shown in figure 3(*b*). In this plot, red circles show the experimental measured values with error bars, and the blue curve shows the fit. Due to large errors on the outermost Thomson scattering point (at low plasma density), the value is replaced with a more reasonable value of $T_e \sim 30$ eV (denoted by a red square), informed by Langmuir probe measurements (a value reported for a similar discharge was $T_e = 23$ eV at that position [3]). The IDS diagnostic indicates that ions are initially hotter than electrons, with $T_i > 1$ keV. Over time, the ions cool due to thermalization with electrons and transport losses in this highly collisional plasma. The spatial profile of the ion temperature is unknown because the IDS diagnostic is only a single chord. Therefore, we assume the ion temperature profile follows the same shape as the electron temperature profile and take $T_i = T_e$ as a nominal baseline. At the time we analyze the plasma, relevant also as a possible initial time of compression, ions may still be hotter than electrons. To capture this, we also explore cases with $T_i/T_e > 1$ using linear stability analysis.

Once these smooth radial profiles of density and temperature are found, a new self-consistent Grad–Shafranov equilibrium is computed. Radial profiles of plasma parameters and magnetic equilibrium are then exported to EFIT format. The resulting plasma profiles for the electron temperature (T_e),
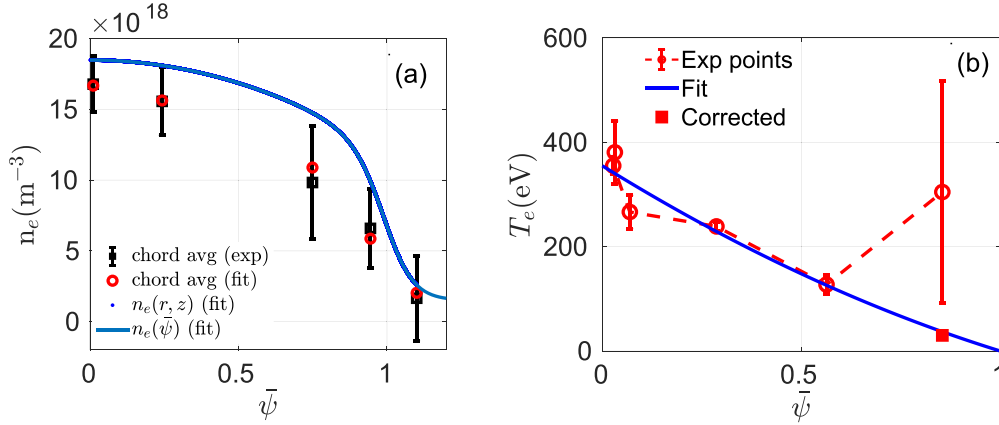
Figure 3. Plasma density profiles from interferometers (left) and temperature from Thomson scattering diagnostics (right) as a function of normalized poloidal flux $\bar{\psi}$ fitted using a forward model. The left panel also shows the experimental data for the chord average density (black squares with error bars) and corresponding best-fit synthetic values (red circles), plotted at the value of $\bar{\psi}$ corresponding to the deepest penetration of that chord into the plasma. As expected for a monotonic density profile, the plotted experimental and fit chord averages lie below the density profile curve because the chord average density is smaller than the density at the deepest penetration along the chord.
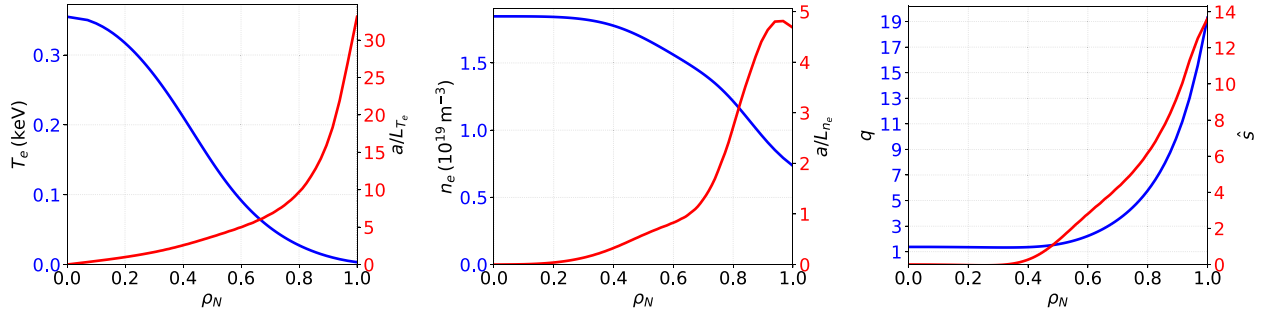

Figure 4. Plasma input profiles as a function of the normalized toroidal flux coordinate, ρ_{N}, for electron temperature (T_{e}) and its normalized gradient ($a/L_{T_{\mathrm{e}}}$) (left), electron density (n_{e}) and its gradient ($a/L_{n_{\mathrm{e}}}$) (middle), and safety factor (q) and its gradient ($\hat{s}$) (right), for the PI3 discharge 18669 at $t = 5$ ms.

electron density (n_{e}), and safety factor (q) as a function of ρ_{N} are shown in figure 4. The normalized logarithmic gradients of these input quantities are also plotted in the figure. These profiles are used to calculate the input parameters for gyrokinetic analysis in this work.

3. Simulation setup and input parameters

This study focuses on a PI3 discharge 18669 at $t = 5$ ms with the goal of characterizing transport at this particular time. The linear and nonlinear gyrokinetic simulations are performed at four radial locations $r/a = 0.60$, $r/a = 0.65$, $r/a = 0.70$ and $r/a = 0.75$ using CGYRO [14, 15], which is an Eulerian gyrokinetic code used to study micro-instabilities and turbulence in toroidal plasmas. Here, r/a is the flux surface minor radius normalized to the minor radius of the LCFS [23], denoted by a. Simulations are performed assuming two species (deuterium and electron) and no impurity species, considering electromagnetic effects by including parallel magnetic vector potential fluctuations ($\delta A_{||}$) and parallel magnetic field fluctuations ($\delta B_{||}$), and collisions.

We define the magnetic geometry using the Miller parametrization [23, 24]. To accurately treat collision effects in high-collisionality regimes of PI3 plasmas, we employ the Sugama collision operator [25, 26]. In PI3, Z_{eff} is determined by measuring the intensity of visible bremsstrahlung emission. Around 5 ms, it typically indicates that the PI3 plasma is clean, with $Z_{\mathrm{eff}} < 2$. Therefore, for the simulations presented here, a flat $Z_{\mathrm{eff}} = 1$ profile was assumed as a starting point. We note that moderate levels of low-Z impurities have previously been found to have only small impacts on the linear stability of JET tokamak plasmas [27].

The experimental input profiles shown in figure 4 are used to calculate the local input parameters for this analysis, listed in table 2. The normalized logarithmic gradient scale lengths for density and temperature are calculated as $a/L_n = -(a/n)(\partial n/\partial r)$, $a/L_T = -(a/T)(\partial T/\partial r)$, where the normalizing length a is the plasma minor radius at the LCFS, T is the temperature, n is the density and r is the flux surface minor radius defined as $r = (R_{\max} - R_{\min})/2$, with $R_{\max}$ and $R_{\min}$ being the maximum and minimum radial coordinate of the flux surface, respectively. The flux surface major radius R_0 is defined as $R_0 = (R_{\max} + R_{\min})/2$. The inter-particle collision rate is defined using a dimensionless electron collision

Table 2. Input parameters for the PI3 discharge 18669 at 5 ms for the four normalized radial locations r/a. Here, $A = R_0/a$ is the aspect ratio at the flux tube position, q the safety factor, $\hat{s} = (r/q)\mathrm{d}q/\mathrm{d}r$ is the magnetic shear, κ the elongation, δ the triangularity, and ζ the squareness. The plasma parameters (ν_e^*, Ω_i, $\omega = c_s/a$, $\rho^* = \rho_s/a$) are calculated using effective magnetic field B_{unit} values and assuming $T_i/T_e = 1.0$.

r/a	0.60	0.65	0.70	0.75
ρ_N	0.51	0.55	0.60	0.65
T_e (keV)	0.14	0.11	0.093	0.071
n_e ($10^{19}\,\mathrm{m}^{-3}$)	1.68	1.63	1.57	1.50
B_{unit} (T)	0.47	0.49	0.52	0.57
a/L_{Te}	3.79	4.37	4.98	5.77
a/L_{ne}	0.60	0.70	0.82	0.98
$\beta_{e,\mathrm{unit}}$ (%)	0.43	0.30	0.21	0.13
$A = R_0/a$	1.40	1.39	1.38	1.36
q	1.61	1.86	2.23	2.78
$\hat{s}$	1.43	2.11	2.81	3.55
κ	1.35	1.36	1.36	1.37
δ	0.013	0.015	0.018	0.022
ζ	−0.0084	−0.012	−0.017	−0.025
ν_e^*	2.74	3.94	5.95	9.56
Ω_i ($10^7\,\mathrm{s}^{-1}$)	2.26	2.38	2.53	2.74
ω ($10^5\,\mathrm{s}^{-1}$)	2.25	2.04	1.81	1.58
ρ^* (10^{-3})	9.97	8.55	7.16	5.77

frequency ν_e^*, normalized by a/c_s [14], as:

$$\nu_e^* = \frac{a}{c_s}\nu_{ee} = \frac{a}{c_s}\frac{\sqrt{2\pi}\,e^4 n_e}{m_e^{1/2} T_e^{3/2}}\ln\Lambda \qquad (3)$$

where ν_{ee} is the electron–electron collision frequency, $\ln\Lambda$ is the Coulomb logarithm, and the deuterium sound speed $c_s = \sqrt{T_e/m_D}$ (where T_e is the electron temperature and m_D is the deuterium ion mass). The magnetic field is defined in terms of effective magnetic field strength B_{unit} [28, 29] and computed with reference to a global equilibrium through the relation as $B_{\mathrm{unit}}(r) = (q/r)\partial\psi/\partial r$, where q is the safety factor and ψ is the poloidal flux divided by 2π. The reference plasma beta value is given in CGYRO in terms of an effective electron beta, $\beta_{e,\mathrm{unit}} = 8\pi n_e T_e/B_{\mathrm{unit}}^2$. Moreover, the deuterium ion mass m_D, the equilibrium electron density on the flux surface n_e, and the electron temperature T_e are used as reference parameters for normalization. The pressure gradient entering the Miller parameterization is given by $\beta^* = -(8\pi/B_{\mathrm{unit}}^2)(\mathrm{d}p/\mathrm{d}r)$, where $p = \sum_s n_s T_s$ is the total plasma pressure. The effect of β^* on the drift velocity is complicated, and described in more detail in [28, 30].

PI3 does not have any neutral beams or external momentum injection sources, so toroidal plasma rotation is expected to only have contributions from self-generated intrinsic rotation [31]. Measurements using IDS typically show toroidal velocities around $10\,\mathrm{km\,s}^{-1}$. The toroidal rotation frequency, ω_0, which relates to the toroidal flow velocity as $\mathbf{U}_0 = \omega_0 R^2\nabla\varphi$, influences three local parameters: the Mach number $M = \omega_0 R_0/c_s$, toroidal rotation shear $\gamma_p = -R_0\mathrm{d}\omega_0/\mathrm{d}r$, and $\mathbf{E}\times\mathbf{B}$ shear $\gamma_E = -(r/q)\mathrm{d}\omega_0/\mathrm{d}r$. Given the low rotation velocity, and for simplicity, we assume no toroidal rotation for this analysis, setting M and γ_p to zero. However, we retain a small finite value for the $\mathbf{E}\times\mathbf{B}$ shear parameter, $\gamma_E = 0.005\,c_s/a$, as any actual device inherently will have some finite level of

$\mathbf{E}\times\mathbf{B}$ shear due to intrinsic rotation, even in the absence of an external momentum source. This is large enough to avoid the irrelevant behavior that occurs in simulations at $\gamma_E = 0$, but small enough that it will not otherwise affect turbulence.

Following linear grid convergence tests, the typical grid parameters chosen for our linear analysis are $(N_x, N_\xi, N_\mu, N_\theta) = (12, 12, 8, 24)$, where N_x, N_ξ, N_μ and N_θ are the number of radial, pitch-angle, energy and poloidal grid points, respectively. For some cases, particularly those with small wave numbers ($k_y\rho_s < 0.1$) where tearing-parity unstable modes are present (as discussed later), the radial grid resolution was increased to $N_x = 24$ to achieve eigenfunction convergence. Detailed definitions of the CGYRO numerical resolution parameters can be found in [14].

The numerical resolution parameters for nonlinear runs include a simulation box size with radial and binormal length $(L_x, L_y) = (125, 125)$ in units of the ion Larmor radius. The grid resolution consists of $N_x = 480$ radial and $N_{ky} = 24$ toroidal Fourier modes, with $k_y\rho_s$ ranging from 0.05 to 1.15. The radial wave vectors extend up to $k_x\rho_s = 11.946$ with a resolution of $\Delta(k_x\rho_s) = 0.050$. A high value of N_x was required due to the sensitivity of fluxes to radial resolution. Other resolution parameters are $(N_\xi, N_\mu, N_\theta) = (16, 8, 24)$.

In the next section, we present the linear analysis done to characterize the dominant micro-instabilities potentially responsible for turbulent fluxes in the nonlinear phase.

4. Linear stability analysis and identification of micro-instabilities

Linear stability analysis is first performed to identify the dominant micro-instabilities present in these plasmas to understand the characteristics of turbulence that are responsible for energy transport.
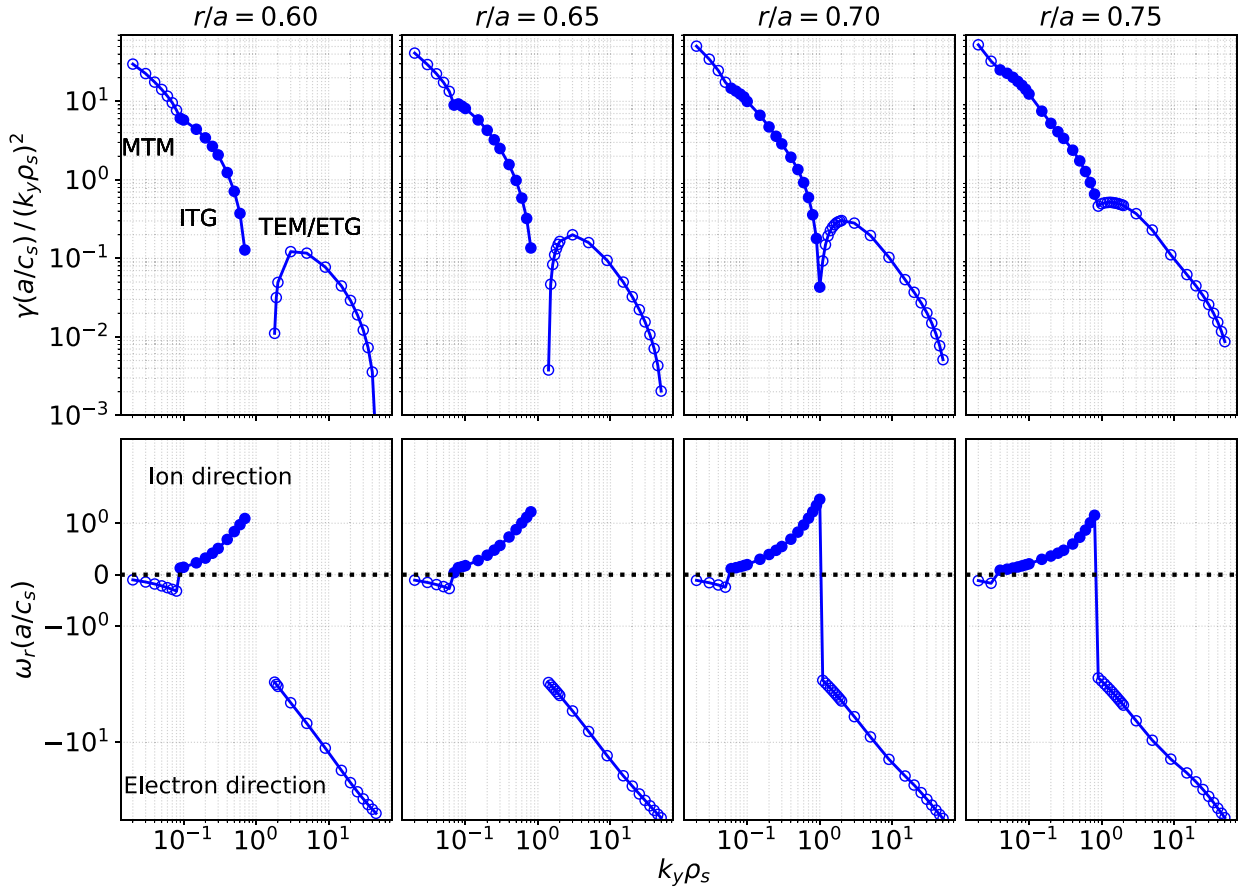
Figure 5. Linear growth rate, normalized to binormal wave-number $(k_y\rho_s)^2$ (top), and real frequency (bottom) spectra as a function of binormal wave-number $k_y\rho_s$ at various radial locations $r/a = 0.60$, $r/a = 0.65$, $r/a = 0.70$, and $r/a = 0.75$, for the PI3 discharge 18669 at $t = 5$ ms. The positive (negative) sign of frequency indicates ion (electron) diamagnetic drift direction, represented by closed (open) marker symbols, respectively.

Figure 5 plots the linear growth rates and real frequency spectra of the most unstable linear mode over the wavenumber range $0.02 < k_y\rho_s < 50$ at the radial locations $r/a = 0.60, 0.65, 0.70, 0.75$. We have chosen here to normalize linear growth rates by $(k_y\rho_s)^2$ to better highlight the trend of the long-wavelength microtearing mode (MTM) branch and improve the readability of the curves. Although not customary, this normalization is reminiscent of the mixing-length transport scaling, γ/k_y^2, and illustrates the potential contribution of the MTM to the nonlinear flux. Here, k_y denotes the binormal wave vector, and $\rho_s = c_s/\Omega_D$ represents the deuterium Larmor radius, where $\Omega_D = eB_{unit}/m_D c$ is the deuterium cyclotron frequency. In this figure, open (closed) symbols represent the electron (ion) diamagnetic drift direction, respectively.

Interestingly, three distinctly dominant branches can be identified in figure 5: (1) ion-scale unstable modes at longest wavelengths (lowest-k, $k_y\rho_s \leqslant 0.1$) propagating in the electron diamagnetic drift direction, (2) ion-scale unstable modes at long wavelengths (low-k, $0.1 \leqslant k_y\rho_s \leqslant 1.0$) propagating in the ion diamagnetic drift direction, and (3) electron-scale modes at intermediate wavelengths (intermediate-k, $1.0 \leqslant k_y\rho_s \leqslant 2.0$) and shorter wavelengths (high-k, $k_y\rho_s \geqslant 2.0$), propagating in the electron diamagnetic drift direction, as indicated by their

frequency sign. The lowest $k_y\rho_s \leqslant 0.1$ linearly unstable modes are characterized by negative frequencies and have tearing parity in the eigenfunctions, i.e. the even (odd) parity of the vector (electrostatic) potential fluctuations as shown in figure 6(left). A reduction in the electron plasma beta also leads to decreased growth rates, as discussed later in section 6.1. Additionally, their behavior is highly sensitive to the ion-to-electron temperature ratio, with larger linear growth rates observed at higher T_i/T_e values, as discussed in section 6.3. All these signatures suggest these modes as MTMs. It is important to note that for these low wavenumbers the mode structures are elongated along field lines and therefore a high radial resolution was needed (up to 24 radial grid points) to resolve the modes accurately. As shown in figure 5(top), in the spectral region where these long-wavelength MTMs are observed, these long-wavelength MTMs can drive significant heat flux in the nonlinear phase, depending on parameters. In the present case, however, they do not contribute significantly to transport and are suppressed during the nonlinear phase, as discussed later in section 5. The low-k ion-scale unstable modes can be identified as ITG modes, based on their ballooning parity, specifically even (odd) $\delta\phi$ ($\delta A_\parallel$), as shown in the middle plot of figure 6. Furthermore, their identification is supported by stabilization
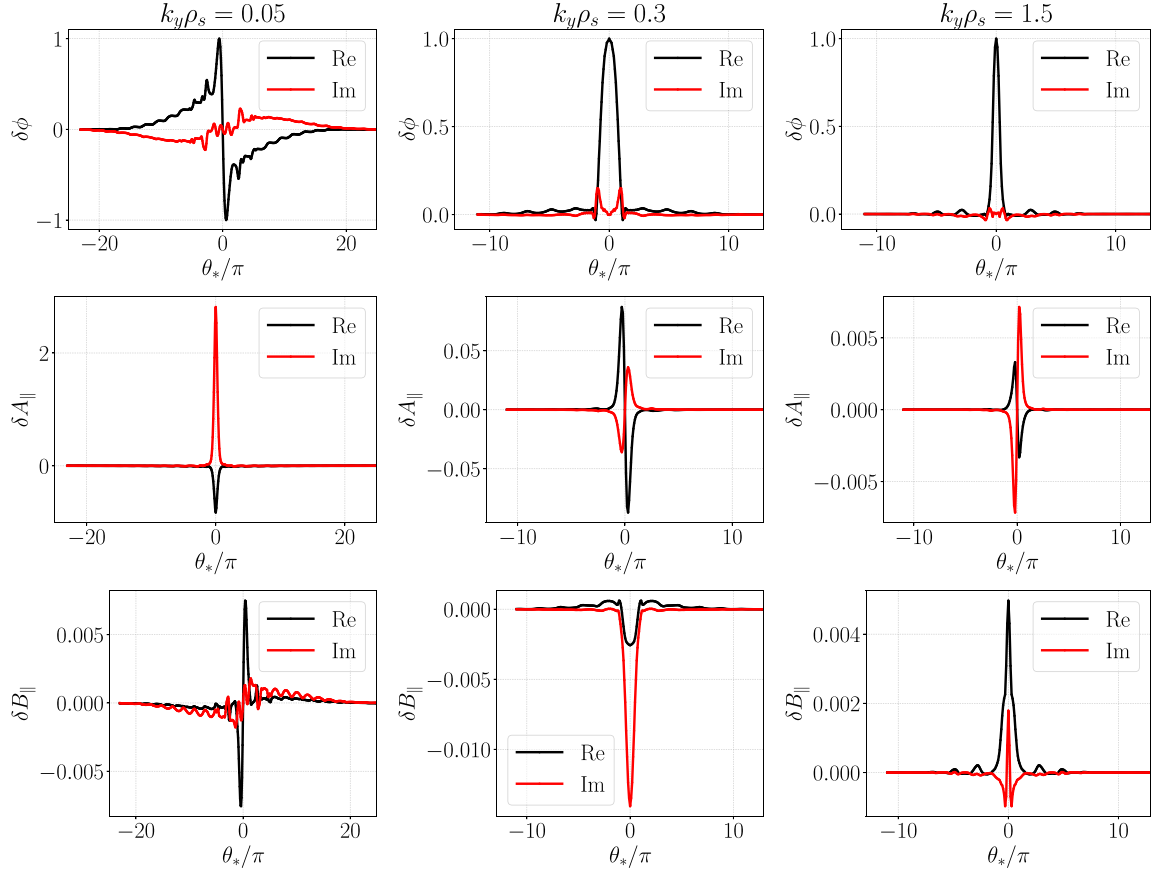
Figure 6. Parallel mode structure of perturbed electrostatic potential $\delta\phi$ (top), magnetic flutter $\delta A_\parallel$ (middle) and magnetic compressional fluctuations $\delta B_\parallel$ (bottom), as a function of poloidal angle θ, for three unstable modes $k_y\rho_i = 0.05$, $k_y\rho_i = 0.3$ and $k_y\rho_i = 1.5$ at $r/a = 0.60$. The black curve represents the real part and the red line indicates the imaginary part of the perturbed fields.

effects due to electron beta (below the KBM threshold), collisionality, and a higher T_i/T_e ratio. These points are discussed in more detail in section 6 of this paper.

The intermediate-*k* and low-*k* modes exhibit an even parity in $\delta\phi$ and an odd parity in $\delta A_\parallel$. However, the intermediate-*k* electron-scale branch is significantly influenced by collisionality, as discussed in section 6.2. These modes can be identified as TEMs due to their ballooning parity, propagation direction, and sensitivity to collisions. Identifying the precise transition point between the TEM and the electron temperature gradient (ETG) unstable modes requires further analysis. Therefore, for simplicity, we refer to the electron-scale unstable branch at $k_y\rho_s \geqslant 1.0$ as the combined TEM/ETG branch throughout this paper. At the outermost radii, the TEM/ETG branch continues to be unstable towards low-*k* until transitioning to the ITG branch. However, at the innermost radii, we find it becomes linearly stable ($\gamma < 0$) at intermediate-*k*, shown as a gap in the plots between the TEM/ETG unstable branch and ITG-unstable branch. In addition, we have checked that turning $\delta B_\parallel$ off for these cases does not produce any significant effect on linear growth rates (plots are not shown here).

Following the linear analysis and identification of dominant unstable modes across the minor radius, the next step is to compute the transport fluxes driven by these unstable modes in

the nonlinear phase. Both ion-scale and electron-scale micro-instabilities are present, spanning long and short wavelengths range at all radial locations. However, including ETG scales would require a prohibitively large simulation domain and intermediate wavelength TEM branches are stable at some locations. Therefore, the nonlinear analysis in the next section focuses exclusively on ion-scale long-wavelength modes. These ion-scale modes contribute most significantly to transport fluxes based on mixing-length estimates as seen in figure 5, and strongly interact with self-generated zonal flows, regulate turbulence, and set transport levels.

5. Nonlinear analysis

In this section, ion-scale nonlinear gyrokinetic simulations are performed at selected radial locations for the nominal parameters to determine the saturated turbulence state and quantify the resulting turbulent fluxes. The simulations span the wavenumber range $0.05 \leqslant k_y\rho_s \leqslant 1.2$. Since turbulence is inherently nonlinear, linear simulations only provide information on growth rates and mode structures. Therefore, nonlinear simulations are essential for capturing turbulence self-regulation by accounting for nonlinear mode coupling, the
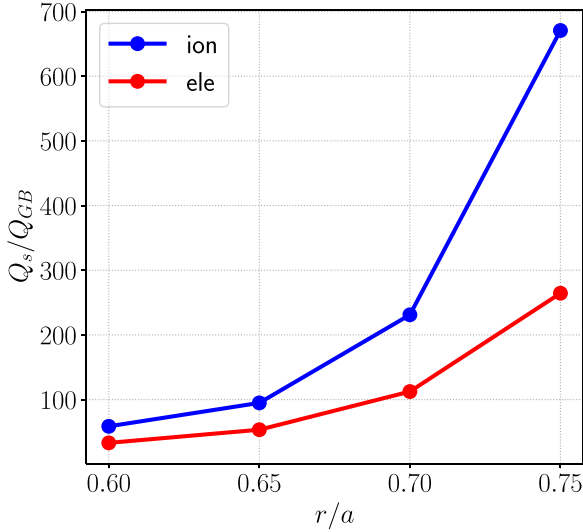
Figure 7. Time-averaged, gyroBohm normalized nonlinear energy fluxes for ions (blue curve) and electrons (red curve) are shown as a function of radial location for the PI3 discharge 18 669 at $t = 5$ ms, corresponding to the reference experimental values.

impact of zonal flows, and cross-scale interactions, which are crucial for accurate transport predictions. Plasma geometry and profiles are held constant during the nonlinear simulations, so that the calculated steady-state turbulence is representative of the slowly evolving plasma state at the time of interest.

Simulations are run for a sufficiently long time to reach a quasi-steady state, ensuring nonlinear convergence after saturation. We ran the simulations to normalized time $(c_s/a)\,t$ in the range 500–2000 as needed to achieve good statistics. The energy fluxes are normalized to reference gyroBohm units: $Q_{GB} = c_s n_e T_e (\rho_s/a)^2$. The total nonlinear turbulent energy flux for a species s is summed over each wavenumber: $Q_s = \sum_{k_y} Q_s^{k_y}$. The total fluxes can be decomposed into individual contributions arising from the electrostatic potential fluctuations ($\delta\phi$), magnetic flutter due to the parallel vector potential fluctuations ($\delta A_\parallel$) and magnetic compressional fluctuations ($\delta B_\parallel$). The simulated energy fluxes, obtained by time-averaging over the last 50% of simulation time, are shown in figure 7. Turbulent energy fluxes increase from inner radius $r/a = 0.60$ to outer radius $r/a = 0.75$. Energy fluxes of similar orders of magnitude have also been reported in earlier studies for conventional tokamaks [32], as well as under ST plasma conditions when $\mathbf{E} \times \mathbf{B}$ shear is negligible [33, 34]. Ion-scale modes are the predominant linearly unstable modes at long wavelengths, but electron energy fluxes remain significant. Specifically, the magnitude of the electron fluxes are on the order of 30%–40% of the ion fluxes. A further observation is that despite relatively large beta and appreciable finite-beta destabilization, the transport is mainly electrostatic (we checked the nonlinear k_y fluxes spectra with individual contributions of $\delta\phi$, $\delta A_\parallel$ and $\delta B_\parallel$). The particle fluxes follow the same trend as energy fluxes, increasing from the inner to the outer radii, with values ranging from $\Gamma_e/\Gamma_{GB} = 7$ at $r/a = 0.60$ to $\Gamma_e/\Gamma_{GB} = 23$ at $r/a = 0.75$.

It is well known that $\mathbf{E} \times \mathbf{B}$ shearing from toroidally symmetric ($n = 0$) zonal flows are the dominant nonlinear saturation mechanism for toroidal drift wave turbulence. The earliest gyrofluid simulations referred to these as *radial modes* [35]. Zonal flows, driven exclusively by nonlinear coupling to finite-n modes, have been extensively studied via numerical simulation [36, 37]. To explore their role in the nonlinear saturation of ITG-dominated PI3 plasmas, we analyzed the amplitude of electrostatic potential fluctuations ($|\delta\phi|$) for nonzonal modes ($k_y > 0$) and zonal modes ($k_y = 0$). The results indicate that zonal flows exhibit a significant amplitude, suggesting that they are the primary nonlinear saturation mechanism in these plasmas (plots are not shown here).

Figure 8 shows two-dimensional contour plots of electrostatic potential fluctuations at the final time step of the simulations. In these plots, x represents the radial direction, and y is the binormal direction. At the inner radii, strong zonal flows suppress radially elongated turbulent eddies (streamers), resulting in a flow-dominated regime with negligible energy fluxes and low turbulent transport. As we move towards the outer radii, radially elongated eddies become dominant, resulting in a streamer-dominated regime region with increased radial transport.

The next step is to explore the parametric dependencies of these linearly unstable modes and the associated nonlinear turbulent fluxes to key parameters that distinguish PI3 from other fusion devices.

6. Scans of input parameters

The present PI3 plasma is different in comparison to core plasmas normally studied with nonlinear gyrokinetic simulations because of the simultaneously large values of plasma beta ($\beta_{e,unit}$) and collisionality (ν_e^*). Motivated by this novelty, in this section we assess the sensitivity of transport to $\beta_{e,unit}$, and ν_e^*. In addition, the ion–electron temperature ratio (T_i/T_e) can be larger than 1, therefore we also analyze its impact on the linear stability of the modes.

6.1. Impact of electron beta

In this section, we present nonlinear simulations at different $\beta_{e,unit}$ values while keeping all other local parameters (i.e. β^* and profile gradients) constant. In CGYRO, this is made possible with an artificial scaling factor $c_{p'}$ [30] such that $\beta^* = -c_{p'}\beta(a/L_T + a/L_n)$[3].

Figure 9 shows the total time-averaged nonlinear energy flux at each selected radial location for different values of $\beta_{e,unit}$. The dominant contribution to both ion and electron energy fluxes here is electrostatic, with small contributions from magnetic flutter and negligible impact from magnetic compression. For example, at $r/a = 0.75$, the magnetic flutter contribution is negative and reduces the total ion energy flux Q_i by $\approx 2\%$ and electron energy fluxes Q_e by $\approx 9\%$,

---

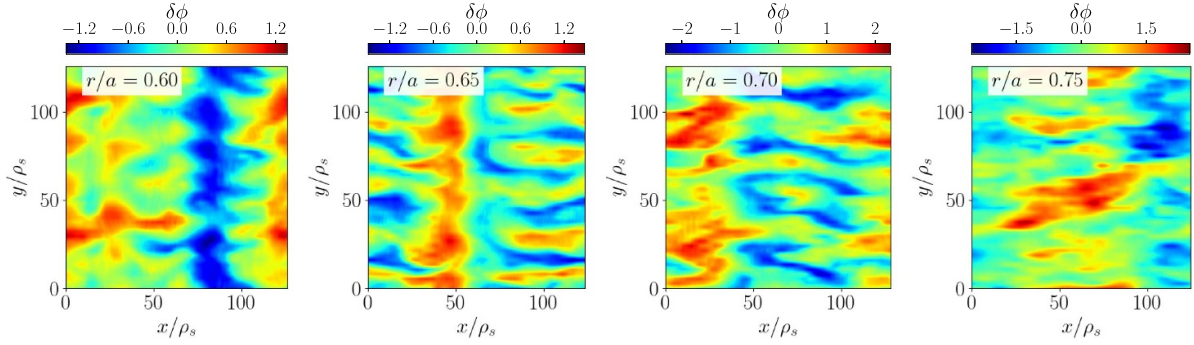[3] This scaling parameter is called `BETASTAR_SCALE` in CGYRO.

Figure 8. Two-dimensional contour plots of the electrostatic potential perturbation ($\delta\phi$) for the baseline case at different radial locations. Each plot is at the last time step of the corresponding simulation.
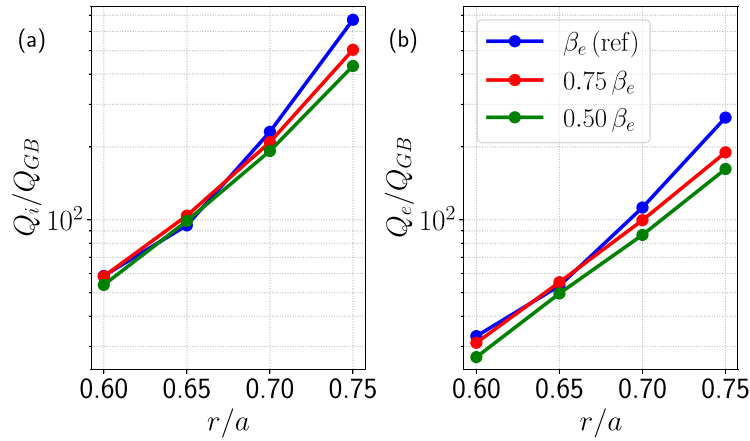

Figure 9. Time-averaged, normalized nonlinear ion (*a*) and electron (*b*) energy fluxes as a function of the normalized minor radius r/a for various $\beta_{e,unit}$ values. The blue curve represents the case with nominal experimental parameters. The red curve shows the results when $\beta_{e,unit}$ is reduced by a factor 4/3, while the green curve for when $\beta_{e,unit}$ is reduced by a factor 2.

whereas the effect of magnetic compression is hardly discernible in either transport channel. At inner radii ($r/a = 0.60$ and $r/a = 0.65$), flux levels remain largely unchanged with increasing $\beta_{e,unit}$, indicating a weaker dependence on $\beta_{e,unit}$. However, at outer radii ($r/a = 0.70$ and $r/a = 0.75$), increasing $\beta_{e,unit}$ significantly enhances transport. This destabilization arises solely from $\beta_{e,unit}$ in Ampère's law. Reducing $\beta_{e,unit}$ by half decreases the fluxes at $r/a = 0.75$ by about 50% and leads to slight reductions at $r/a = 0.70$. In all simulations fluxes are bursty in the nonlinear phase.

The nonlinear beta destabilization is opposite to the linear behavior, as illustrated in figure 10, where the linear growth rate spectra for different values of $\beta_{e,unit}$ are shown. In this plot, we divide linear growth rates by $k_y \rho_s$ to again improve clarity of the MTM branch. Because drift wave eigenvalues are $\mathcal{O}(k_y)$ in the limit $k_y \to 0$, this normalization serves as a useful check that the long-wavelength numerical solutions are well-behaved. As beta increases, the linear growth rate for ITG modes ($k_y \rho_s \approx 0.3$) decreases at the innermost radii below a critical threshold of KBMs but remains unchanged at the outermost radii ($r/a = 0.70$ and $r/a = 0.75$). The stabilizing effect of finite $\beta_{e,unit}$ is commonly attributed to magnetic field line bending induced by electromagnetic perturbations as plasma beta increases. This linear stabilization was

historically expected to carry over to nonlinear transport, suppressing turbulence fluxes [38–40]. Over time, the role of $\beta_{e,unit}$ on nonlinear electromagnetic simulation emerged as a complex topic because of the difficulty of obtaining well-converged simulations. While $\beta_{e,unit}$ was shown to somewhat suppress the linear growth rates of ITG instabilities, reductions in energy transport were lower than expected. More frequently, transport increases explosively without saturation [38] when beta exceeds a critical threshold that is below the MHD critical β (also called KBM threshold, a kinetic equivalent of MHD critical beta limit). Further, the radial motion of electrons in stochastic magnetic fields created by finite $\delta A_\parallel$ causes stochastic transport of electrons [41, 42]. This effect is especially noticeable in the linear regime at long wavelengths ($k_y \rho_s \leqslant 0.1$ in figure 10), where decreasing β_e reduces the linear growth rate of MTM modes.

To further investigate the $\beta_{e,unit}$-dependence, we present the nonlinear energy flux spectra in figure 11. As shown in the figure, MTMs generally do not contribute significantly to transport fluxes across all radial locations in the nonlinear phase (even though they are present in the linear spectra), except at the outermost radii, where there is a small negative contribution from magnetic flutter. At $r/a = 0.75$, the spectrum peaks at the longest wavelength mode ($k_y \rho_s = 0.05$),
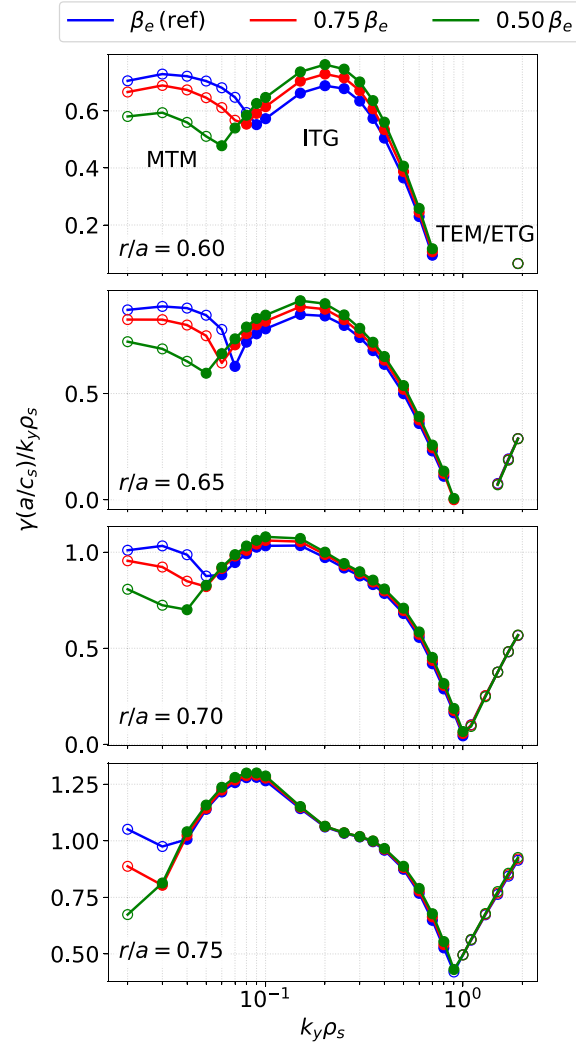
Figure 10. Linear growth rate spectra normalized to $k_y\rho_s$ for various beta values at different radial locations. Here, the blue curve represents the experimental (reference) parameters, the red curve shows the results when $\beta_{e,unit}$ is reduced by a factor of 4/3 from its experimental value, and the green curve where $\beta_{e,unit}$ is reduced by a factor of 2. Open (closed) markers correspond to electron (ion) diamagnetic drift direction.

contributing notably to the total energy flux. However, this peak is primarily due to the electrostatic component, while the magnetic flutter contribution is small, negative, and slightly reduces the total electron energy flux. The presence of a flutter contribution suggests that MTMs are linearly subdominant unstable modes at this radial location and wavenumber, as linear initial-value calculations capture only the fastest-growing mode. Subdominant MTMs at low $k_y\rho_s$ have been previously observed in JET hybrid H-mode plasmas [43], though in the present case they are not dominant in the nonlinear phase. Moreover, significant contributions to both nonlinear ion and electron energy fluxes at all radii come from long-wavelength ITG modes. The nonlinear saturation and suppression of MTMs and their contribution to magnetic flutter transport, especially in spherical tokamaks is an active area of research on its own [16, 33, 44], and it is clear that further work is needed to understand the suppression mechanisms in PI3 plasmas.

6.2. Impact of collisionality

In this section, we explore the sensitivity to collisionality to understand its impact on PI3 plasmas. As discussed in section 2.1, the most notable characteristic of this plasma is high collisionality compared to contemporary large tokamaks, primarily due to its relatively low temperature. In this highly collisional regime the TEM is strongly stabilized by detrapping of trapped electrons.

Figure 12 plots the energy fluxes for varying values of ν_e^*. The fluxes increase as ν_e^* decreases. Specifically, at $r/a = 0.65$ and $r/a = 0.70$, the energy flux for both ions and electrons increases by a factor of 1.3 to 1.5 when collisionality is reduced by a factor of 4/3, and increases by a factor of 2 when ν_e^* is reduced by a factor of 2. Further in, at $r/a = 0.60$, energy fluxes increase slightly by a factor of 1.2 and 2 when ν_e^* is reduced by a factor of 4/3 and 2, respectively. In all cases, the energy flux is dominated by the electrostatic contributions,
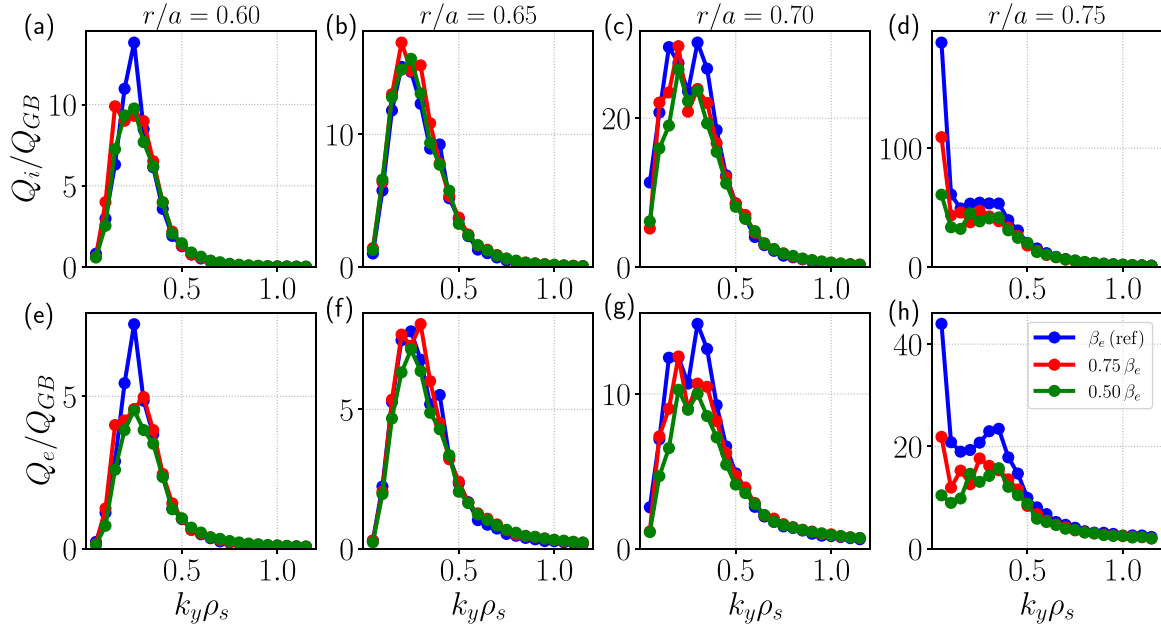
Figure 11. Nonlinear k_y spectra of the normalized ion (top) and electron (bottom) energy fluxes averaged over time window of last 50% of simulation time at $r/a = 0.60$ (*a*), (*e*), $r/a = 0.65$ (*b*), (*f*), $r/a = 0.70$ (*c*), (*g*) and $r/a = 0.75$ (*d*), (*h*). Here, the blue curve corresponds to the reference parameters, the red curve when $\beta_{e,unit}$ is reduced by a factor of 4/3 from its experimental value, and the green curve when $\beta_{e,unit}$ is reduced by a factor of 2.
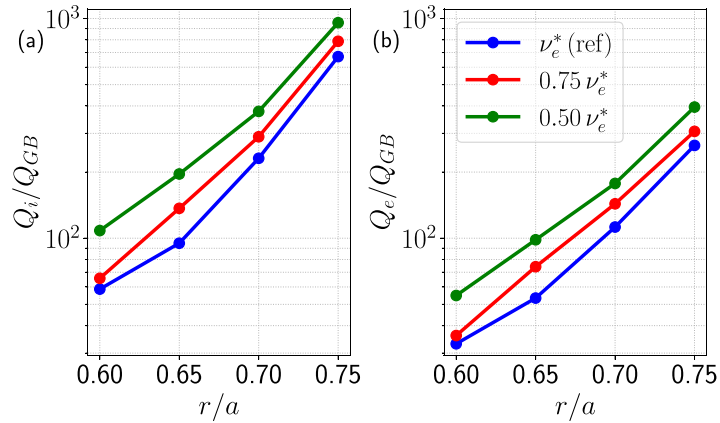
Figure 12. Time-averaged nonlinear ion (*a*) and electron (*b*) energy fluxes at four radial locations for different collisionality ν_e^* values. The blue curve represents the nominal value of ν_e^*, the red curve shows a reduction by a factor of 4/3, and the green curve by a factor of 2.

with negligible contribution from magnetic flutter. The degree of destabilization is the same for both ion and electron channels. This behavior is consistent with the well-known effect that electron collisions reduce the fraction of trapped electrons, thereby weakening the ITG and TEM drive and reducing the growth rate [14].

Figure 13 presents the corresponding linear results. The value of ν_e^* has a significant effect on reducing MTM and ITG linear growth rates, in some regions completely suppressing intermediate wavelength TEM modes at innermost radii. As ν_e^* decreases, the linear growth rates of both ITG and MTM modes increase. This trend is reflected in the nonlinear energy fluxes shown in figure 12, where an increase in energy fluxes is observed with decreasing collisionality. The linear growth rate spectrum indicates that some TEM modes which were stable

for the nominal parameters become unstable at $r/a = 0.60$ and 0.65 when collisionality is reduced.

6.3. Impact of temperature ratio

In this section, we assess the linear sensitivity of unstable modes to the ion-to-electron temperature ratio T_i/T_e. We consider the range $1.0 \leqslant T_i/T_e \leqslant 1.4$ based on observed conditions in PI3 discharges at the selected time. In these scans all other parameters are kept constant but β^* is allowed to vary when T_i/T_e is changed. In conventional tokamaks, it has been observed that increasing T_i/T_e significantly enhances plasma performance in electrostatic simulations, improving plasma confinement by raising the stability thresholds for both ion and
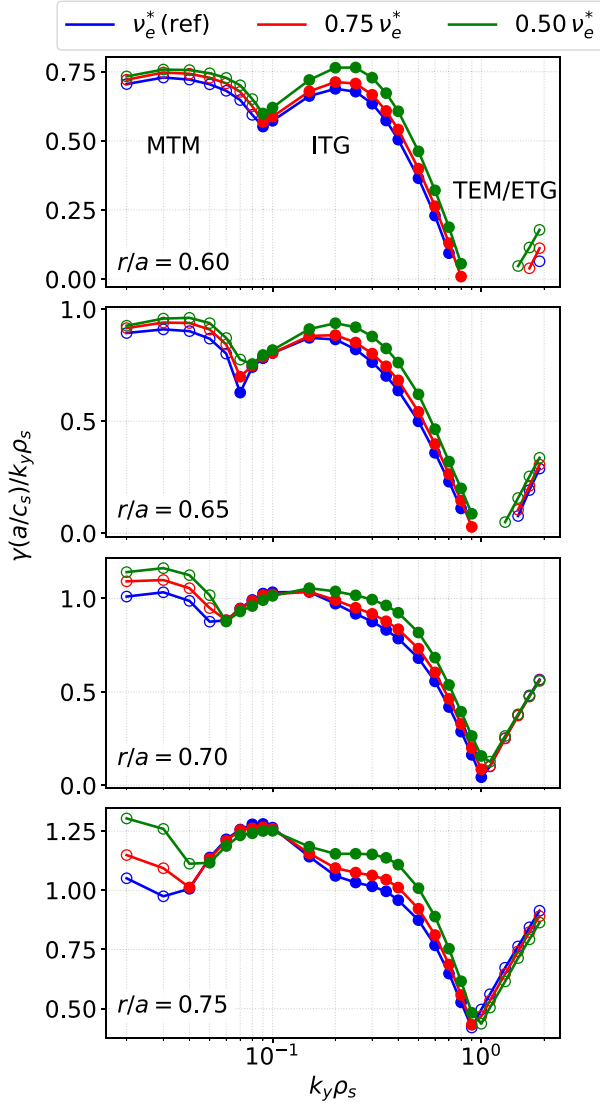
Figure 13. Linear growth rate spectra normalized to $k_y\rho_s$ as a function of binormal wave-number $k_y\rho_s$ with scans of the normalized collisionality ν_e^* at various radial locations. The blue curve represents the reference case, red and green for the case when ν_e^* is reduced by a factor of 4/3 and 2. Here, open (closed) markers correspond to the electron (ion) diamagnetic drift direction.

Figure 14. Linear growth rate spectra normalized to $k_y\rho_s$ as a function of binormal wave-number $k_y\rho_s$ when temperature ratio T_i/T_e is varied from the reference value at selected radial locations. The blue curve represents the reference case $T_i/T_e = 1.0$, whereas the red and green curves correspond to increased temperature ratios of $T_i/T_e = 1.2$ and $T_i/T_e = 1.4$, respectively. Open (closed) markers correspond to the electron (ion) diamagnetic drift direction.

electron modes [45, 46]. However, these results can change substantially in the presence of electromagnetic effects.

Figure 14 shows the results of varying the ratio T_i/T_e in linear simulations. The net effect of increasing T_i/T_e has opposing effects on the two branches: it stabilizes ion-driven ITG modes while destabilizing electron-driven TEM/ETG modes. The impact of T_i/T_e on turbulent transport is complex and depends on the dominant instability and the normalized density gradient [46], which can result in higher or lower instability thresholds. While ITG stabilization with higher T_i/T_e is well-established, the effect on TEM/ETG modes is more sensitive to density gradients and collisionality [47]. In the present high-collisionality, finite density gradient case, we find that increasing T_i/T_e leads to a destabilization of TEM/ETG modes. Notably, we also observe a stronger destabilization of the long
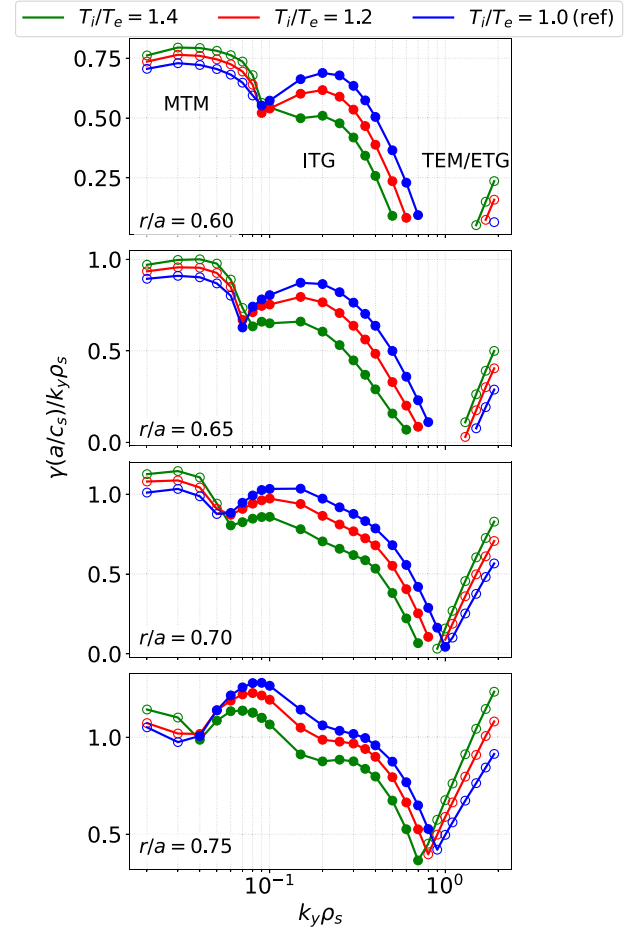
wavelength MTM branch at higher T_i/T_e ratios, which could contribute to heat fluxes in the nonlinear regime depending on the plasma conditions.

We attempted nonlinear simulations for a case with a high T_i/T_e=1.4 and observed periods of unbounded flux, indicating qualitatively different confinement behavior. We suspect the excitation of long wavelength MTM modes at higher T_i/T_e ratio could be the possible reason for this behavior, though further work is required to explore this.

7. Comparison of turbulent energy fluxes with neoclassical fluxes

In this section, simulated turbulent energy fluxes from CGYRO are compared with neoclassical fluxes calculated using NEO, a multi-species drift-kinetic neoclassical code [18, 26]. The results, plotted for ion and electron energy fluxes in physical units for reference parameters and various parameter scans, are shown in figure 15. For the baseline parameters, turbulent energy fluxes exceed the neoclassical ones across all
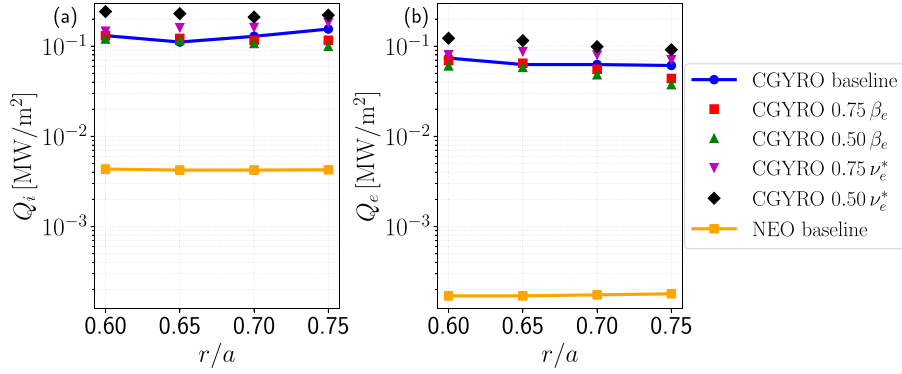
Figure 15. Comparison of simulated nonlinear turbulent ion (*a*) and electron (*b*) energy fluxes calculated using CGYRO and neoclassical values from NEO. The blue circle (●) and line represents the turbulent fluxes from CGYRO for the baseline parameters, while the red square (■) corresponds to the case where $\beta_{e,unit}$ is reduced by a factor of 4/3, and the green triangle (▲) shows the results when $\beta_{e,unit}$ is reduced by a factor of 2. The magenta triangle (▼) indicates results when ν_e^* is reduced by a factor of 4/3, and the black diamond (◆) shows the flux when ν_e^* is reduced by a factor of 2. Finally, the orange square (■) and line marks the neoclassical values from NEO.

radii. Even with reductions in $\beta_{e,unit}$ and ν_e^* by factors of 4/3 and 2, respectively, turbulent energy fluxes remain significantly higher than the neoclassical values.

8. Summary and conclusions

This paper has presented the first gyrokinetic transport analysis to characterize the dominant micro-instabilities and associated levels of thermal transport in small-aspect-ratio spherical tokamak plasmas developed as targets for compression in General Fusion's MTF technology. The analysis focused on the PI3 spherical tokamak plasma discharge 18669 at time $t = 5$ ms. PI3 plasmas, as MTF target plasmas, have relatively low temperature and high collisionality compared to conventional tokamak plasmas. These plasma conditions result from the formation of the plasma by CHI without any external auxiliary heating system.

Local linear and nonlinear gyrokinetic analysis was carried out using the gyrokinetic code CGYRO at four selected radial locations: $r/a = 0.60$, 0.65, 0.70, and 0.75. Simulations were performed for a realistic geometry, including collisions, electromagnetic effects ($\delta A_\parallel$ and $\delta B_\parallel$), and a small $\mathbf{E} \times \mathbf{B}$ shear value ($\gamma_E = 0.005 c_s/a$), consistent with the absence of an external momentum injection source.

The linear analysis showed that ITG modes are the dominant micro-instability at the long wavelength (ion scale) across all radial locations. A transition to TEMs occurs at intermediate wavelengths $k_y\rho_s \geqslant 1.0$ at the outer radii $r/a = 0.70$ and 0.75. On the other hand, at the inner radii $r/a = 0.60$ and 0.65 TEMs are linearly stable, which is attributed to the high collisionality in these plasmas.

At the longest wavelengths ($k_y\rho_s \leqslant 0.1$), linearly unstable MTMs with tearing parity (even parity in vector potential fluctuations) and propagating in the electron drift direction were observed. Turning off magnetic compressional fluctuations ($\delta B_\parallel$) in the linear analysis has a negligible impact on

linear growth rates. Below a critical KBM threshold, increasing $\beta_{e,unit}$ stabilizes the dominant micro-instability at inner radii by reducing growth rates, while having little effect on ITG modes at outer radii. Notably, higher $\beta_{e,unit}$ enhances the growth of tearing-parity modes, in contrast to its stabilizing impact on ITG modes. Systematic scans of parametric dependencies were performed on key input parameters, including $\beta_{e,unit}$, ν_e^* and T_i/T_e. These scans reveal that while linear growth rates may vary within the tested parameter ranges, the dominant micro-instability remains unchanged. Interestingly, the effect of T_i/T_e depends on the type of dominant instability; increasing T_i/T_e from unity stabilizes ITG modes, while it destabilizes TEM/ETG branches and long-wavelength MTMs.

The nonlinear simulations showed that saturated turbulent energy fluxes are primarily driven by long-wavelength ITG modes. Interestingly, although MTMs are linearly unstable, they are suppressed nonlinearly. Various saturation mechanisms for microtearing turbulence have been proposed, including the role of zonal fields [33] and shear flows [41], but a complete understanding of MTM suppression in nonlinear regimes for spherical tokamaks remains an open question and requires further investigation in the present case. The turbulence was found to be electrostatic in nature for both ion and electron transport channels, with negligible contributions from $\delta B_\parallel$ and magnetic flutter ($\delta A_\parallel$), except at outer radii (e.g. $r/a = 0.75$) where the magnetic flutter contribution is small and negative, reducing the total ion energy flux Q_i by approximately 2% and the electron energy flux Q_e by about 9%. At this location, the spectrum of the heat flux in the nonlinear simulations peaks at the longest wavelength ($k_y\rho_s = 0.05$), which is an electrostatic mode. While beta stabilization is observed in the linear phase at all radii, in the nonlinear phase beta has a destabilizing effect on turbulence, although without the runaway effect normally seen in the analysis of conventional tokamak plasmas.

Reducing collisionality by a factor of two leads to an increase of the nonlinear energy fluxes by a similar factor. Overall, collisionality has a more robust impact than beta in reducing turbulent transport fluxes. Nonlinear simulations for

a case with a higher $T_i/T_e = 1.4$ proved challenging, resulting in periods of unbounded flux, suggesting qualitatively different behavior.

We have not explored plasma shaping in this study, though it can be optimized in MTF plasmas. Variations in plasma shape such as elongation, triangularity, and their gradients can significantly affect turbulent transport. In conventional tokamaks, elongation and its gradient have been shown to stabilize energy transport driven by ITG and TEM instabilities [48]. Similarly, negative triangularity has been found to positively impact energy confinement time [49]. However, plasma shaping effects on transport and stability in small-aspect-ratio plasmas remain largely unexplored. Moreover, extrapolating from this analysis, it seems likely that during compression and heating, the plasma is likely to transition into regimes of turbulent transport dominated by other micro-instabilities. Consequently, the effects of beta, collisionality, and plasma shaping should also be investigated in these regimes.

An example of the novelty of these results compared to standard spherical tokamaks lies in the observed differences in dominant transport mechanisms. For instance, linear gyrokinetic calculations for NSTX have shown that at the much higher temperatures achieved there, energy transport is dominated by electron-scale modes, such as hybrid TEM/KBM and also contributions from MTM, while ITG modes are suppressed by strong $\mathbf{E} \times \mathbf{B}$ shear generated by neutral beam injection. The profiles also appear to be constrained below the KBM threshold [17]. This contrasting result is in agreement with the experimental determination that in high-β H-mode discharges, ion thermal transport is near neoclassical levels [50, 51], and despite the gross similarity in many geometric parameters between NSTX and PI3 (see table 1). As demonstrated in this work, the relatively increased electron dissipation observed in PI3 plasmas seems to prevent electron-scale modes, and thus the electron transport channel, from becoming the dominant contributor to turbulent thermal transport.

Acknowledgments

ORCID iDs

N. Kumar ⓘ 0000-0001-8693-555X
G. Avdeeva ⓘ 0000-0001-7072-7967
J. Candy ⓘ 0000-0003-3884-6485
M. Reynolds ⓘ 0000-0001-5880-2290
E. Belli ⓘ 0000-0001-7947-2841
C.P. McNally ⓘ 0000-0002-2565-6626

References

[1] Laberge M. 2019 Magnetized target fusion with a spherical tokamak J. Fusion Energy 38 199–203
[2] Howard S.J. et al 2024 Measurement of spherical tokamak plasma compression in a PCS-16 magnetized target fusion experiment Nucl. Fusion 65 016029
[3] Antony A., Carbajal L., Rognlien T.D., Umansky M.V., Froese A., Howard S., Ribeiro C., Ivanov R., Dunlea C. and McNally C.P. 2025 Boundary plasma studies for a spherical tokamak with lithium walls Nucl. Mater. Energy 42 101885
[4] Tancetti A. et al 2025 Thermal energy confinement time of spherical tokamak plasmas in PI3 Nucl. Fusion 65 036043
[5] Carle P.J.F., Howard S. and Morelli J. 2013 High-bandwidth polarimeter for a high density, accelerated spheromak Rev. Sci. Instrum. 84 083509
[6] Carle P., Froese A., Wong A., Howard S., O'Shea P. and Laberge M. 2016 Polarimeter for the General Fusion SPECTOR machine Rev. Sci. Instrum. 87 11E104
[7] Young W.C. and Parfeniuk D. 2016 Thomson scattering at general fusion Rev. Sci. Instrum. 87 11E521
[8] Frieman E.A. and Chen L. 1982 Nonlinear gyrokinetic equations for low frequency electromagnetic waves in general plasma equilibria Phys. Fluids 25 502–8
[9] Sugama H. and Horton W. 1998 Nonlinear electromagnetic gyrokinetic equation for plasmas with large mean flows Phys. Plasmas 5 2560–73
[10] White A.E. et al (Alcator C-Mod Team) 2013 Multi-channel transport experiments at Alcator C-Mod and comparison with gyrokinetic simulations Phys. Plasmas 20 056106
[11] Holland C., White A.E., McKee G.R., Shafer M.W., Candy J., Waltz R.E., Schmitz L. and Tynan G.R. 2009 Implementation and application of two synthetic diagnostics for validating simulations of core tokamak turbulence Phys. Plasmas 16 052301
[12] Freethy S.J., Görler T., Creely A.J., Conway G.D., Denk S.S., Happel T., Koenen C., Hennequin P. and White A.E. (ASDEX Upgrade Team) 2018 Validation of gyrokinetic simulations with measurements of electron temperature fluctuations and density-temperature phase angles on ASDEX Upgrade Phys. Plasmas 25 055903
[13] Nakata M., Honda M., Yoshida M., Urano H., Nunami M., Maeyama S., Watanabe T.-H. and Sugama H. 2016 Validation studies of gyrokinetic ITG and TEM turbulence simulations in a JT-60U tokamak using multiple flux matching Nucl. Fusion 56 086010
[14] Candy J., Belli E.A. and Bravenec R.V. 2016 A high-accuracy Eulerian gyrokinetic solver for collisional plasmas J. Comput. Phys. 324 73–93
[15] Candy J., Sfiligoi I., Belli E., Hallatschek K., Holland C., Howard N. and D'Azevedo E. 2019 Multiscale-optimized plasma turbulence simulation on petascale architectures Comput. Fluids 188 125–35
[16] Guttenfelder W., Candy J., Kaye S.M., Nevins W.M., Bell R.E., Hammett G.W., LeBlanc B.P. and Yuh H. 2012 Scaling of linear microtearing stability for a high

collisionality national spherical torus experiment discharge
Phys. Plasmas **19** 022506

[17] Clauser C.F., Guttenfelder W., Rafiq T. and Schuster E. 2022
Linear ion-scale microstability analysis of high and
low-collisionality NSTX discharges and NSTX-U
projections *Phys. Plasmas* **29** 102303

[18] Belli E.A. and Candy J. 2008 Kinetic calculation of
neoclassical transport including self-consistent electron and
impurity dynamics *Plasma Phys. Control. Fusion*
50 095010

[19] Meyer H. *et al* (the MAST and NBI Teams) 2009 Overview
of physics results from MAST *Nucl. Fusion*
49 104017

[20] Menard J.E. *et al* 2017 Overview of NSTX upgrade initial
results and modelling highlights *Nucl. Fusion*
57 102006

[21] Maggi C.F. *et al* 2007 Characteristics of the H-mode pedestal
in improved confinement scenarios in ASDEX upgrade,
DIII-D, JET and JT-60U *Nucl. Fusion* **47** 535

[22] de Vries P.C. *et al* 2009 Internal transport barrier dynamics
with plasma rotation in JET *Nucl. Fusion* **49** 075007

[23] Arbon R., Candy J. and Belli E.A. 2020 Rapidly-convergent
flux-surface shape parameterization *Plasma Phys. Control.
Fusion* **63** 012001

[24] Miller R.L., Chu M.S., Greene J.M., Lin-Liu Y.R. and
Waltz R.E. 1998 Noncircular, finite aspect ratio, local
equilibrium model *Phys. Plasmas* **5** 973–8

[25] Sugama H., Watanabe T.-H. and Nunami M. 2009 Linearized
model collision operators for multiple ion species plasmas
and gyrokinetic entropy balance equations *Phys. Plasmas*
16 112503

[26] Belli E.A. and Candy J. 2012 Full linearized Fokker—Planck
collisions in neoclassical transport simulations *Plasma
Phys. Control. Fusion* **54** 015015

[27] Kumar N. 2021 Analysis of turbulent transport in the central
part of high-confinement tokamak plasmas Aix-Marseille
Université (available at: http://www.theses.fr/
2021AIXM0038)

[28] Candy J. 2009 A unified method for operator evaluation in
local Grad—Shafranov plasma equilibria *Plasma Phys.
Control. Fusion* **51** 105009

[29] Waltz R.E. and Miller R.L. 1999 Ion temperature gradient
turbulence simulations and plasma flux surface shape *Phys.
Plasmas* **6** 4265–71

[30] Belli E.A. and Candy J. 2010 Fully electromagnetic
gyrokinetic eigenmode analysis of high-beta shaped
plasmas *Phys. Plasmas* **17** 112314

[31] deGrassie J.S., Burrell K.H., Baylor L.R., Houlberg W. and
Lohr J. 2004 Toroidal rotation in DIII-D in electron
cyclotron heating and Ohmic H-mode discharges *Phys.
Plasmas* **11** 4323–31

[32] Marinoni A., Austin M.E., Candy J., Chrystal C., Haskey S.R.,
Porkolab M., Rost J.C. and Scotti F. 2024 Nonlinear
gyrokinetic modelling of high confinement negative
triangularity plasmas *Nucl. Fusion* **64** 086045

[33] Giacomin M., Kennedy D., Casson F.J., Ajay C.J.,
Dickinson D., Patel B.S. and Roach C.M. 2024 On
electromagnetic turbulence and transport in step *Plasma
Phys. Control. Fusion* **66** 055010

[34] Roach C.M. *et al* 2009 Gyrokinetic simulations of spherical
tokamaks *Plasma Phys. Control. Fusion* **51** 124020

[35] Waltz R.E., Kerbel G.D. and Milovich J. 1994 Toroidal gyro
Landau fluid model turbulence simulations in a nonlinear
ballooning mode representation with radial modes *Phys.
Plasmas* **1** 2229–44

[36] Dimits A.M. *et al* 2000 Comparisons and physics basis of
tokamak transport models and turbulence simulations *Phys.
Plasmas* **7** 969

[37] Waltz R.E. and Holland C. 2008 Numerical experiments on the
drift wave—zonal flow paradigm for nonlinear saturation
Phys. Plasmas **15** 122503

[38] Candy J. 2005 Beta scaling of transport in microturbulence
simulations *Phys. Plasmas* **12** 072307

[39] Pueschel M.J., Kammerer M. and Jenko F. 2008 Gyrokinetic
turbulence simulations at high plasma beta *Phys. Plasmas*
15 102310

[40] Pueschel M.J. and Jenko F. 2010 Transport properties of
finite-β microturbulence *Phys. Plasmas* **17** 062307

[41] Guttenfelder W., Candy J., Kaye S.M., Nevins W.M., Wang E.,
Bell R.E., Hammett G.W., LeBlanc B.P., Mikkelsen D.R.
and Yuh H. 2011 Electromagnetic transport from
microtearing mode turbulence *Phys. Rev. Lett.* **106** 155004

[42] Nevins W.M., Wang E. and Candy J. 2011 Magnetic
stochasticity in gyrokinetic simulations of plasma
microturbulence *Phys. Rev. Lett.* **106** 065003

[43] Kumar N., Camenen Y., Benkadda S., Bourdelle C., Loarte A.,
Polevoi A.R. and Widmer F. (JET Contributors) 2021
Turbulent transport driven by kinetic ballooning modes in
the inner core of JET hybrid H-modes *Nucl. Fusion*
61 036005

[44] Hatch D.R., Pueschel M.J., Jenko F., Nevins W.M., Terry P.W.
and Doerk H. 2012 Origin of magnetic stochasticity and
transport in plasma microturbulence *Phys. Rev. Lett.*
108 235002

[45] Weiland J., Asp E., Garbet X., Mantica P., Parail V., Thomas P.,
Suttrop W. and Tala T. (the EFDA-JET Contributors) 2005
Effects of temperature ratio on JET transport in hot ion and
hot electron regimes *Plasma Phys. Control. Fusion* **47** 441

[46] Alessandro Casati C.B., Garbet X. and Imbeaux F. 2008
Temperature ratio dependence of ion temperature gradient
and trapped electron mode instability thresholds *Phys.
Plasmas* **15** 042310

[47] Romanelli M., Bourdelle C. and Dorland W. 2004 Effects of
high density peaking and high collisionality on the
stabilization of the electrostatic turbulence in the Frascati
Tokamak Upgrade *Phys. Plasmas* **11** 3845–53

[48] Kinsey J.E., Waltz R.E. and Candy J. 2007 The effect of
plasma shaping on turbulent transport and E×B shear
quenching in nonlinear gyrokinetic simulations *Phys.
Plasmas* **14** 102306

[49] Camenen Y., Pochelon A., Behn R., Bottino A., Bortolon A.,
Coda S., Karpushov A., Sauter O. and Zhuang G. (the TCV
Team) 2007 Impact of plasma triangularity and
collisionality on electron heat transport in TCV l-mode
plasmas *Nucl. Fusion* **47** 510

[50] Kaye S.M. *et al* 2007 Scaling of electron and ion transport in
the high-power spherical torus NSTX *Phys. Rev. Lett.*
98 175002

[51] Kaye S.M., Gerhardt S., Guttenfelder W., Maingi R.,
Bell R.E., Diallo A., LeBlanc B.P. and Podesta M. 2013
The dependence of H-mode energy confinement and
transport on collisionality in NSTX *Nucl. Fusion* **53** 063005